Astronomy & Astrophysics manuscript no. aa2014_24129
July 28, 2014
©ESO 2014

arXiv:1407.6944v1 [astro-ph.HE] 25 Jul 2014

Searching for highly obscured AGN in the XMM-Newton serendipitous source catalog

A. Corral[1], I. Georgantopoulos[1], M.G. Watson[2], S.R. Rosen[2], E. Koulouridis[1], K.L. Page[2], P. Ranalli[1], G.Lanzuisi[1], G. Mountrichas[1], A. Akylas[1], G.C. Stewart[2], and J.P. Pye[2]

[1] Institute for Astronomy, Astrophysics, Space Applications, and Remote Sensing (IAASARS), National Observatory of Athens (NOA, Greece)
e-mail: acorral@noa.gr
[2] Department of Physics & Astronomy, University of Leicester, Leicester, LE1 7HR, UK

Received , ; accepted ,

ABSTRACT

The majority of active galactic nuclei (AGN) are obscured by large amounts of absorbing material that makes them invisible at many wavelengths. X-rays, given their penetrating power, provide the most secure way for finding these AGN. The *XMM-Newton* serendipitous source catalog, of which 3XMM-DR4 is the latest version, is the largest catalog of X-ray sources ever produced; it contains about half a million detections. These sources are mostly AGN. We have derived X-ray spectral fits for very many 3XMM-DR4 sources ($\gtrsim$ 114 000 observations, corresponding to $\sim$ 77 000 unique sources), which contain more than 50 source photons per detector. Here, we use a subsample of $\simeq$ 1000 AGN in the footprint of the SDSS area (covering 120 deg^2) with available spectroscopic redshifts. We searched for highly obscured AGN by applying an automated selection technique based on X-ray spectral analysis that is capable of efficiently selecting AGN. The selection is based on the presence of either a) flat rest-frame spectra from a simple power-law fit; b) flat observed spectra from an absorbed power-law fit; c) an absorption turnover, indicative of a high rest-frame column density; or d) the presence of an Fe Kα line with a large equivalent width (EW >500 eV). We found 81 highly obscured candidate sources. Subsequent detailed manual spectral fits revealed that 28 of them are heavily absorbed by column densities higher than 10^{23} cm^{-2}. Of these 28 AGN, 15 are candidate Compton-thick AGN on the basis of either a high column density, consistent within the 90% confidence level with $N_H > 10^{24}$ cm^{-2}, or a large equivalent width (>500 eV) of the Fe Kα line. Another six are associated with near-Compton-thick AGN with column densities of $\sim 5\times10^{23}$ cm^{-2}. A combination of selection criteria a) and c) for low-quality spectra, and a) and d) for medium- to high-quality spectra, pinpoint highly absorbed AGN with an efficiency of 80%.

Key words. X-rays: general – X-rays: diffuse background – Surveys – Galaxies: active

1. Introduction

The hard X-ray surveys (2-10 keV) performed with the *Chandra*[1] and *XMM-Newton*[2] missions provide the most unbiased census of the accretion history in the Universe because they can penetrate large amounts of dust and gas. The deep 4Ms *Chandra* survey reached a surface density of $\sim$ 20 000 active galactic nuclei (AGN) deg^{-2} (e.g., Xue et al. 2011). Most X-ray AGN are obscured by high column densities (N_H), typically above 10^{22} cm^{-2} (e.g., Tozzi et al. 2006, Akylas et al. 2006). In contrast, optical quasi-stellar object (QSOs) surveys yield surface densities lower by about two orders of magnitude because they are prone to obscuration, although [OIII] selection diminishes the effect of this bias (Bongiorno et al. 2010). Significant improvements have been made in mid-IR surveys, which now reach similar surface densities as X-ray surveys (e.g., Brown et al. 2006, Delvecchio et al. 2014) because they can easily detect luminous QSOs. Nevertheless, they can hardly separate obscured and, in general, low-luminosity AGN from star-forming galaxies where the host-galaxy colors dominate the spectral energy distribution (e.g., Barmby et al. 2006, Georgantopoulos et al. 2008). However, even the very efficient hard X-ray surveys fail to detect a fraction of highly obscured AGN ($N_H > 10^{23}$ cm^{-2}), and in particular, AGN with column densities above 1.5×10^{24} cm^{-2}. The latter are the Compton-thick (CT) AGN, where the primary mechanism for X-ray attenuation is Compton scattering on electrons instead of photoelectric absorption, which is the primary absorption mechanism at lower column densities.

Several authors have suggested that the number of CT sources can be constrained by using the spectrum of the extragalactic X-ray light, the X-ray cosmic background (XCB). CT AGN are a basic ingredient of XCB synthesis models (e.g., Gilli et al. 2007, Treister et al. 2009, Ballantyne et al. 2011, Akylas et al. 2012) because they are needed to reproduce the broad peak at 20-30 keV observed in the XCB (Frontera et al. 2007, Moretti et al. 2009). However, different authors reported very different CT AGN fractions, the exact *intrinsic* fraction remaining uncertain by at least a factor of two, ranging from about 10% of the total AGN population up to 35%. This is most likely caused by the strong parameter degeneracy on XCB synthesis models, as shown in Akylas et al. (2012). Owing to ultra-hard X-ray surveys above 10 keV performed with *Swift*[3] and *INTEGRAL*[4], CT AGN are commonly observed in the local Universe and represent 4-20% of local active galaxies at

[1] http://chandra.harvard.edu/
[2] http://xmm.esac.esa.int/
[3] http://swift.gsfc.nasa.gov/
[4] http://sci.esa.int/integral/

energies 15-200 keV down to a flux limit of 10^{-11} erg cm^{-2} s^{-1} (see Burlon et al. 2011 and references therein). *NuSTAR*[5] is currently extending these searches to about two orders of magnitude deeper (Alexander et al. 2013, Lansbury et al. 2014).

Still, the identification of CT AGN in the commonly used 2-10 keV band is difficult. Attempts to identify CT AGN have been made primarily in deep X-ray surveys with *Chandra* and *XMM-Newton* missions. These efforts include those of Tozzi et al. (2006), Comastri et al. (2011) and Georgantopoulos et al. (2013), all in the Chandra Deep Field South (CDFS), the region of the sky with the deepest X-ray observations both in *Chandra* and *XMM-Newton*. An alternative approach is to cover a large area of the sky albeit at a relatively bright flux limit, and at lower redshifts. According to the XCB population synthesis models of e.g., Akylas et al. (2012), the fraction of CT sources among all AGN increases by a factor of three as the flux limit, in the 2-10 keV band, decreases from $\approx 2 \times 10^{-14}$ erg cm^{-2}s^{-1}, the effective flux limit of the 120 deg^2 serendipitous XMM/SDSS survey (Georgakakis & Nandra 2011), to $5{\times}10^{-17}$ erg cm^{-2}s^{-1}, the flux limit of the 0.12deg^2, 4Ms survey in the Chandra deep field south. This means that the XMM/SDSS, composed of $\sim$ 40 000 X-ray sources detected over an area of $\sim$ 122 deg^2, contains a factor of a couple of hundred more CT AGN than the CDFS. Given that Brightman & Ueda (2012) reported 40 CT AGN, or CT candidates, in the 4Ms CDFS survey, this implies that there are about 8 000 CT AGN within the XMM/SDSS survey.

Here, we present a fully automated selection technique of highly obscured ($N_H > 10^{23}$ cm^{-2}), and CT AGN ($N_H > 10^{24}$ cm^{-2}). The most reliable way of identifying highly obscured AGN and CT AGN from X-ray surveys is to manually fit their X-ray spectra to derive the actual intrinsic column density. However, in large X-ray samples, this method is extremely time consuming, and less reliable color-selection techniques are often used. We developed a highly efficient selection technique (efficiency $\sim$ 80% in selecting highly obscured AGN), which makes use of automated spectral fits to pinpoint this type of sources, and can be applied to large X-ray surveys. To develop this technique, we used X-ray spectral data from the *XMM-Newton* serendipitous source catalog (Watson et al. 2009), and applied automated X-ray spectral fits implemented for the *XMM-Newton* spectral-fit database (Corral et al. 2014). The test sample of AGN used to develop this technique is composed of more than 1000 AGN with spectroscopic redshifts extracted from the XMM/SDSS-DR7 (Sloan Digital Sky Survey Data release 7) cross-correlation presented in Georgakakis & Nandra (2011).

2. XMM-Newton serendipitous source catalog

The *XMM-Newton* serendipitous source catalog is the largest catalog of X-ray sources built to date (Watson et al. 2009). In its latest release, the 3XMM-Newton *Data Release* 4 (hereafter 3XMM-DR4) contains photometric information for more than 500 000 source detections corresponding to $\sim$ 370 000 unique sources. As part of the catalog construction, time series and spectra were also extracted if the source counts collected in the European Photon Imaging Camera (EPIC) were > 100 (more than 120 000 detections). As a result, 3XMM-DR4 contains X-ray source and background spectra as well as ancillary matrices for more than $\sim$ 85 000 individual sources. The redistribution matrices used in this work are the canned matrices provided by the *XMM-Newton* Science Operations Centre (SOC). Note that the EPIC camera is composed of three detectors: one pn and two MOS cameras[6]. The count limit of 100 counts adopted in spectral extraction during the construction of the 3XMM-DR4 catalog corresponds to the addition of source (background-subtracted) counts in the three detectors. For a detailed description of the catalog and the spectral extraction see http://xmmssc-www.star.le.ac.uk/Catalogue/3XMM-DR4/.

[5] http://www.nustar.caltech.edu/

3. XMM-Newton spectral-fit database

The *XMM-Newton* spectral-fit database is an European Space Agency (ESA) funded project aimed at the construction of a catalog of automated spectral-fitting results corresponding to all sources for which spectral data are available within the 3XMM-DR4. The main goal is to provide the astronomical community with a tool to construct large and representative samples of X-ray sources according to their spectral properties, rather than to their photometric ones.

The resulting spectral-fit database contains one row per source and observation, listing source information, spectral-fit output parameters and errors, as well as fluxes and additional information about the goodness of fit for every model applied. A detailed description of the database and the different spectral models applied is presented on the project web page: http://xraygroup.astro.noa.gr/Webpage-prodec/index.html.

3.1. Automated spectral fitting

The spectral-fit database is constructed by using automated spectral fits. The software used to perform the spectral fits is `XSPEC v12.7` (see Arnaud 1996), the standard package for X-ray spectral analysis. 3XMM-DR4 source spectra are grouped to one count per bin, and Cash statistics, implemented as C-stat in `XSPEC`, are used to fit the data. This statistic was selected instead of the more commonly used χ^2 statistics to optimize the spectral fitting for low-quality spectra. Grouping to one count per bin in combination with C-stat has been proven to work very well for low-count spectra down to 40 net (background-subtracted) counts (Krumpe et al. 2008). All available instruments and exposures for a single observation of a source are fitted together. All parameters for different instruments are tied together except for a relative normalization, which accounts for the differences between different flux calibrations for different EPIC instruments (MOS1, MOS2, and pn), which it is left free to vary. The distribution of ratios between the normalizations for the different instruments is shown in Fig. 1. The plotted values correspond to the sample used in this work, described in Sect. 4.1, and they were obtained from an absorbed power-law model fit.

A lower limit on the number of counts in each individual spectrum was imposed to ensure a minimum quality on the spectral fits. As a result, not all 3XMM-DR4 spectra, but only spectra corresponding to a single EPIC instrument, with more than 50 source counts in the full band (0.5-10 keV) were used in the spectral fits. Parameter errors were computed and reported in the database at the 90% confidence level (Δ C = 2.706 in one interesting parameter). The final *XMM-Newton* spectral-fit

[6] http://xmm.esac.esa.int/external/xmm_user_support/documentation/technical/EPIC/index.shtml

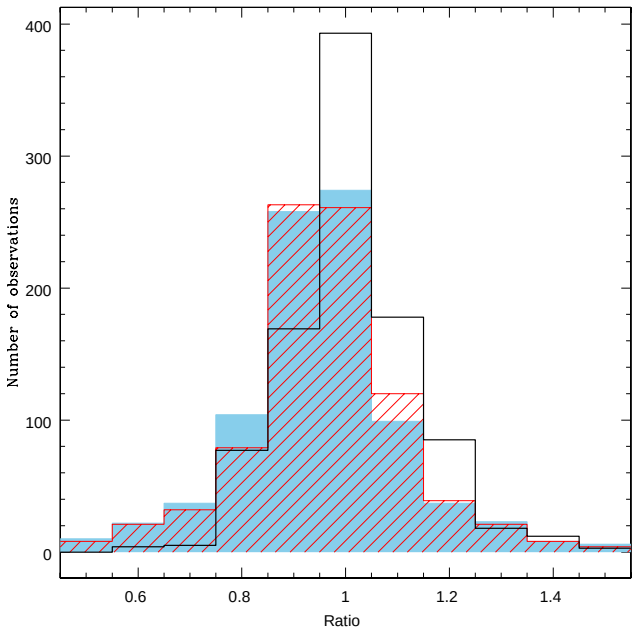

Fig. 1. Distribution of normalization ratios for the three EPIC instruments: MOS2-to-MOS1 ratio (empty histogram); pn-to-MOS1 ratio (line shaded histogram); and pn-to-MOS2 ratio (filled histogram).

database contains spectral-fitting results for $\gtrsim$ 114 000 detections corresponding to $\sim$ 77 000 unique sources.

Three simple (absorbed power-law, absorbed thermal, and absorbed black-body models) and three more complex (absorbed double power-law, absorbed thermal plus power-law, and absorbed black-body plus power-law) models were implemented within the spectral-fitting pipeline according to the number of counts in the X-ray spectra. Simple models were applied to sources in 3XMM-DR4 with more than 50 counts, and more complex models only to sources with more than 500 counts. These models were selected and optimized to reproduce the most commonly observed X-ray spectral shapes among different astronomical sources. Unlike the spectral fits used in this work (see Sect. 4.2), only X-ray data were used to construct the full spectral-fit database, that is, no information about the source type or its redshift was used during the automated spectral fits.

C-stat statistics lacks an estimate of the goodness of fit. To provide a proxy of the fit quality in the spectral-fit database, goodness of fit was estimated by using the `XSPEC` command `goodness`. This command performs a number of simulations and returns the fraction of the simulations that results in a better fit statistic. Therefore, for high return values of this command, a spectral fit with an N% `goodness` value can be rejected at the N% confidence level. The reduced χ^2 value, obtained by using C-stat as the fitting statistic, is also included in the database.

Sometimes, the automated fitting process is unable to constrain all the variable parameters during the error computation. In these cases, spectral parameters that cannot be constrained are fixed during the spectral fits. The fixed values of the parameters depend on the data quality, the complexity of the model, and the energy band in which the spectral fit is being performed. In the case of simple models, the parameter that cannot be constrained is fixed to the value obtained by fitting a model that only includes the corresponding model component in the energy band that encompasses the maximum contribution of that component. For example, if the power-law photon index cannot be constrained in the case of the absorbed power-law model, its value is fixed to that obtained by fitting a power-law model without absorption in the hard (2-10 keV) band. The input parameter values for complex models, which are also the values the parameters are fixed to if they cannot be constrained, are the ones obtained from the spectral-fitting results of the simple models.

A complete description of the XMM-newton spectral-fit database and the automated spectral-fitting pipeline will be presented in a forthcoming paper (Corral et al., in preparation).

4. Automated selection of highly absorbed candidates

4.1. Test sample

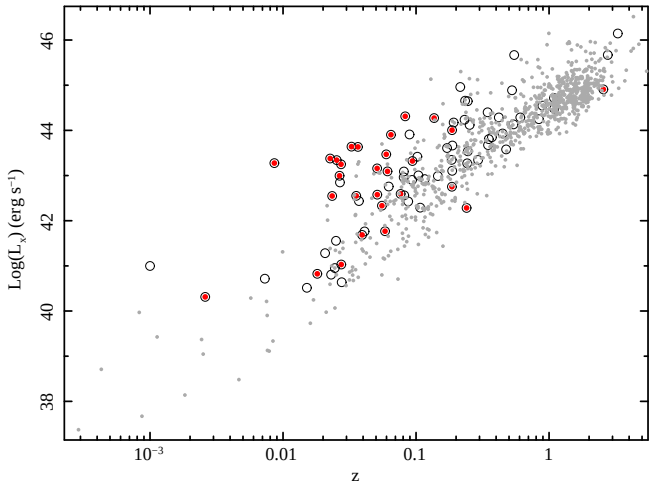

Fig. 2. Intrinsic 2-10 keV luminosity versus redshift for the full XMM/SDSS spectroscopic sample (gray dots), the sample of the 81 highly absorbed candidates based on the automated spectral-fit selection (circles), and the 28 confirmed highly absorbed sources (filled circles, see text).

To test our automated selection technique, a sample of AGN was extracted from the XMM/SDSS cross-correlation presented in Georgakakis & Nandra (2011). The initial sample is composed of **1015 sources** sources, detected in the hard band (2-8 keV), for which spectral data within the 3XMM-DR4 catalog with more than 50 counts in at least one EPIC instrument, and spectroscopic redshifts within SDSS-DR7 were available. Figure 2 presents the intrinsic luminosities (in the 2-10 keV energy band) as a function of redshift for this sample. Observed fluxes (in 2-10 keV) and total collected counts per source (in 0.5-10 keV) distributions are shown in Figs. 3 and 4, respectively.

4.2. Automated spectral-fit models

The spectral models implemented for the spectral-fit database were modified to include the effects of redshift and Galactic absorption. Spectral-fitting results corresponding to all sources within the XMM/SDSS-DR7 cross-correlation detected in the hard (2-8 keV) band ($\sim$ 14 000 sources) can be accessed

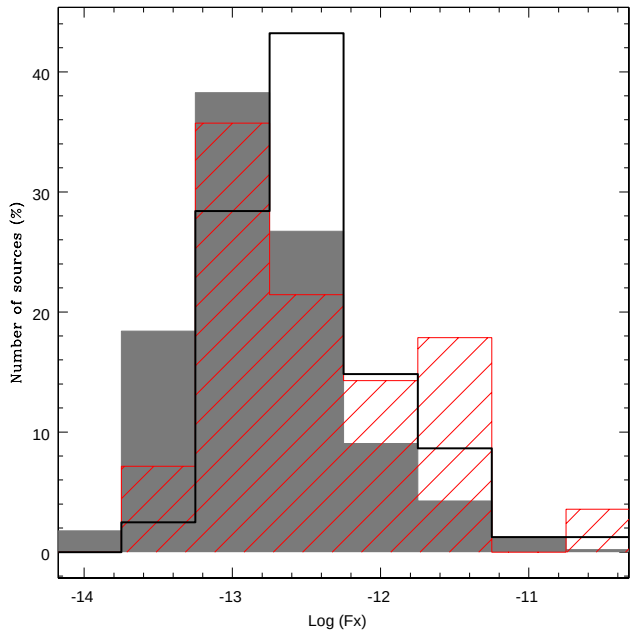

Fig. 3. Observed 2-10 keV flux distribution (in c.g.s units) for the full XMM/SDSS spectroscopic sample (filled histogram), the sample of highly absorbed candidates (empty histogram), and the highly absorbed sources (line-shaded histogram, see text).

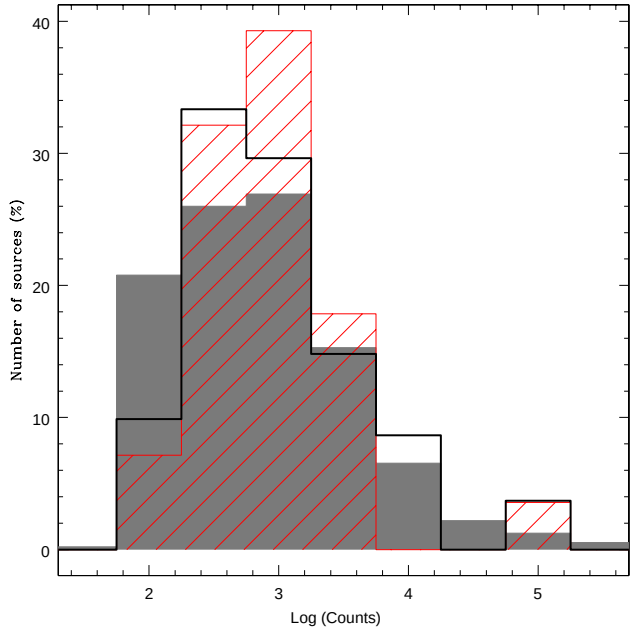

Fig. 4. Distribution of total counts per source in the 0.5-10 keV band for the full XMM/SDSS spectroscopic sample (filled histogram), the sample of highly absorbed candidates (empty histogram), and the highly absorbed sources (line-shaded histogram, see text).

at the spectral database web page. Although many sources within the 3XMM-DR4 catalog have been observed multiple times, the spectral-fitting pipeline has been designed to fit each observation separately. Therefore, automated spectral-fitting results are available for each individual observation of each source.

For the purpose of this work, four new models were implemented by adding a narrow Gaussian emission line to the absorbed power-law model and the three complex models. This line is intended to represent Fe Kα emission line, the most commonly observed emission line in AGN X-ray spectra. For spectra with fewer than 100 counts above 2 keV, the line energy and width were fixed to 6.4 keV, and 0.1 keV, respectively. For a larger number of counts, the central energy was allowed to vary within the 6.3-6.9 keV range. Models including this emission line were considered as complex models, and as such, they were only applied to sources with more than 500 counts in at least one observation.

4.3. Selection of highly absorbed candidates

The automated spectral-fitting pipe-line, given the limited number of spectral models that have been implemented, and the lack of goodness of fit, was not designed to decide which model was the best-fit model among those tried for each observation, but to obtain the best possible representation of the spectral shape. Nevertheless, acceptable fits were found for $\sim$ 80% of the sources in the full XMM-Newton spectral-fit database, in terms of `goodness` values. This is not often the case for highly absorbed sources. This type of AGN usually displays complex X-ray spectra that are only poorly fitted by using the rather simple models used for the automated fits. However, the automated fitting results can be used as a proxy of the actual spectral shape, even if the model is an unacceptable fit, and that information can be used to select highly absorbed sources.

To obtain the most reliable selection technique, four different automated selection criteria were explored that accommodate the spectral characteristics most often shown by highly absorbed AGN. In all cases, and to be able to apply our method to all the sources in the sample with enough number of counts, automated spectral-fitting results were used regardless of the goodness of fit for the model under consideration.

A source was considered a highly absorbed candidate if its automated spectral-fitting results fulfilled any of the following criteria (at least in one observation, for sources with multiple observations):

1. **FLATH sample (67 sources)**, flat spectrum in the hard (2-10 keV) rest-frame band: We selected sources with a measured photon index in the 2-10 rest-frame band < 1.4 at the 90% confidence level, excluding absorption. This photon index was derived during the automated spectral fits as part of the absorbed power-law model.
2. **FLATA sample (33 sources)**, flat spectrum in the total (0.5-10 keV) band: We selected sources with a measured photon index < 1.4 at the 90% confidence level from the absorbed power-law fit.
3. **HABS sample (32 sources)**, highly absorbed sources (intrinsic $N_H > 5{\times}10^{23}$ cm^{-2}) from the absorbed power-law fit. We did not take into account the errors in this case since, as pointed out before, highly absorbed sources are usually not acceptably fitted by a simple absorbed power-law model, but we can use a high column density value as an indication of actual heavy absorption or a complex spectrum. Therefore, it is important to remember that this does not mean that the source is actually highly absorbed, since we are not taking the goodness of this fit into account.
4. **HEW sample (16 sources)**, large equivalent width sources: We selected spectra for which the best-fit model (the one

with the lowest value of goodness) includes a line with equivalent width (EW) > 500 eV at the 90% confidence level. Note that this selection criterion was only applied to sources with more than 500 counts collected in their X-ray spectra, **515 sources** in the full sample.

With the exception of the Fe Kα emission line, all the other selection criteria were chosen so as to pinpoint highly obscured sources by using a very simple spectral model (an absorbed power law, wabs*zwabs*pow in XSPEC notation), and therefore, they can be applied to all sources within our sample with the only limitation that the number of counts is > 50 in at least one detector.

Since the four samples of highly absorbed candidates have sources in common (see Fig. 5), the final sample is composed of **81 sources**. Information about the observations available in 3XMM-DR4 for these sources is listed in Table 4. For sources with multiple observations, all available observations are listed, even if the automated spectral-fitting results classified the source as a highly absorbed candidate in just one of the observations.

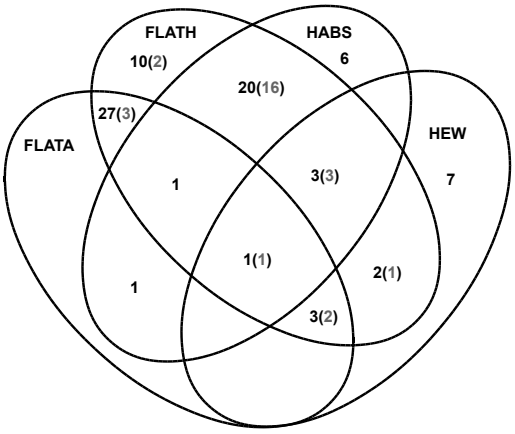

Fig. 5. Venn diagram for the four samples of highly absorbed candidates. Numbers between parenthesis correspond to confirmed highly absorbed AGN according to manual spectral fits (see Sect. 5).

5. Manual testing of the automated selection criteria

After the automated selection, all the available observations within 3XMM-DR4 of the 81 highly absorbed candidates were manually analyzed to check if the sources were in fact highly absorbed ($N_H > 10^{23}$ cm^{-2}). To check for source variability between different observations, the values of the photon index, intrinsic absorption and fluxes were compared by fitting each observation separately. Spectra for the same source and EPIC instrument corresponding to different observations were merged if the parameter values and fluxes were consistent within errors at the 90% confidence level.

The models applied during the manual fits are more complex than the rather simple ones used in the construction of the database. For example, to model the soft emission in highly oscured AGN, we tied together both photon indices when fitting a double power-law model, whereas they are allowed to have different values in the database. In this way, we can separate a scattering component, the soft power-law with the same photon index as the hard one, from an additional thermal component(s), if present. This component(s) can become important in highly obscured AGN at low luminosities because the contribution of the host galaxy to the soft band becomes more and more significant.

The fit statistic used was C-stat, and the models applied during the manual fits are listed below. Since targets were not excluded from our parent sample of 1015 AGN, many of the 81 candidates have been previously analyzed in detail and the results published in the literature, by using more complex models than those we use here. We restricted our spectral fits to our limited set of models to keep our analysis consistent. A source was considered as highly absorbed after the manual fits if the resulting intrinsic column density was higher than 10^{23} cm^{-2} at the 90% confidence level.

- PL (wabs*zwabs*pow): photoelectrically absorbed power law. The absorption components wabs and zwabs (also applicable to the following models) correspond to absorption fixed to the Galactic column density at the source coordinates, and absorption shifted to the source redshift, respectively.
- PL+L (wabs*zwabs*(pow+zgaus)): same as PL, plus a narrow emission line whose central energy is fixed to 6.4 keV rest-frame, and its width to 0.1 keV.
- WAPL (wabs*absori*pow): same as PL, but in this case the redshift absorber is ionized, usually called a warm absorber.
- 2WAPL (wabs*absori*absori*pow): same as WAPL, but including an additional ionized absorber.
- 2WAPL+L (wabs*absori*absori*(pow+zgaus)): same as 2WAPL, plus a narrow emission line defined as in PL+L.
- WAPL+L (wabs*absori*absori*(pow+zgaus)): same as WAPL, plus a narrow emission line defined as in PL+L.
- PL+T (wabs*(zwabs*pow+mekal): same as PL, plus a thermal component.
- PL+T+L (wabs*(zwabs*(pow+zgaus)+mekal): same as PL+T, plus a narrow emission line defined as in PL+L.
- WAPL+T+L (wabs*(absori*(pow+zgaus)+mekal): same as PL+T+L, but substituting the neutral absorber by an ionized one.
- PL+R+L (wabs*(zwabs*(pow+zgaus)+pexrav)): same as PL+R, plus a narrow emission line defined as in PL+L.
- PL+T+R+L (wabs*(zwabs*(pow+zgaus)+pexrav)): same as PL+R+L, plus a thermal component.
- 2PL (wabs*(zwabs*pow+pow)): double power-law model in which the photon indices of both power-law components are tied to the same value. The scattered fraction, that is, the fraction of the intrinsic (power law) emission that is scattered into our line of sight by the absorbing material, is estimated by obtaining the ratio between the normalizations of both power laws.
- PCPL (wabs*zpcfabs*pow): this is in fact functionally the same model as 2PL, but we used this one instead if the scattering fraction for the 2PL model was > 10%, which indicates that the soft power-law component is not scattered emission, but transmitted emission.
- PCPL+L (wabs*zpcfabs*(pow+zgaus)): same as PCPL, plus a narrow emission line defined as in PL+L.
- PCPL+T (wabs*zpcfabs*(pow+mekal)): same as PCPL, plus a thermal component.
- 2PL+L (wabs*(zwabs*(pow+zgaus)+pow)): same as 2PL, plus a narrow emission line defined as in PL+L.
- 2PL+T (wabs*(zwabs*pow+mekal+pow)): same as 2PL, plus a thermal component.

Table 1. Number of AGN manually best-fitted by each model

Model (1)	Candidates (2)	CT (3)	near-CT (4)	H.A. (5)
PL	6	...	...	...
PL+L	8	...	...	...
WAPL	6	...	...	...
2WAPL	1	...	...	...
2WAPL+L	1	...	...	...
WAPL+L	1	...	...	...
PL+T	5	...	...	...
PL+T+L	1	...	...	...
WAPL+T+L	1	...	...	...
PL+R+L	4	3	...	...
PL+T+R+L	1	1	...	...
2PL	5	...	...	1
PCPL	3	...	...	...
PCPL+L	3	...	...	...
PCPL+T	1	...	...	...
2PL+L	8	1	...	...
2PL+T	3	...	1	1
2PL+T+L	21	10	5	3
2PL+2T+L	2	...	...	2

Notes. *Columns:* (1) Model name (see text for details). (2) Number of AGN best-fitted by the model among the 81 highly absorbed candidates. (3) Number of CT AGN best-fitted by the model. (4) Number of near-CT AGN best-fitted by the model. (5) Number of highly absorbed AGN that are not CT or near-CT, best-fitted by the model.

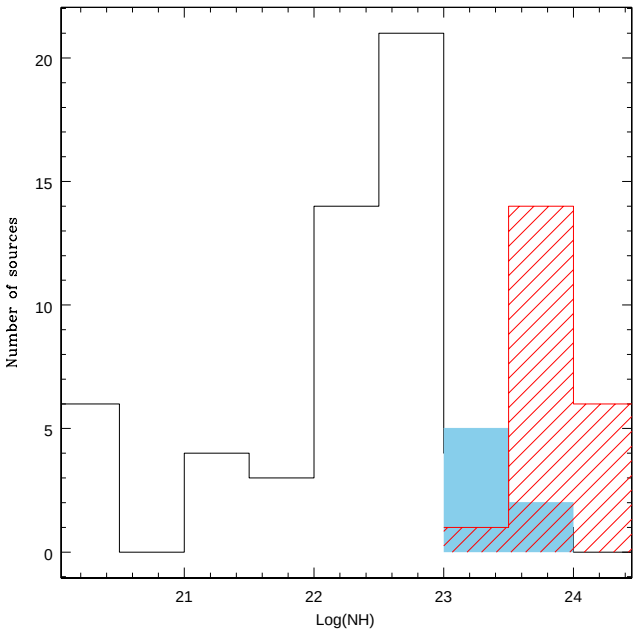

Fig. 6. Column density distribution from the manual analysis for the 81 highly absorbed candidates: the line-shaded histogram correspond to the 21 CT plus near-CT AGN, filled histogram to the 7 highly absorbed but not CT or near-CT AGN, and the empty histogram to the remaining AGN.

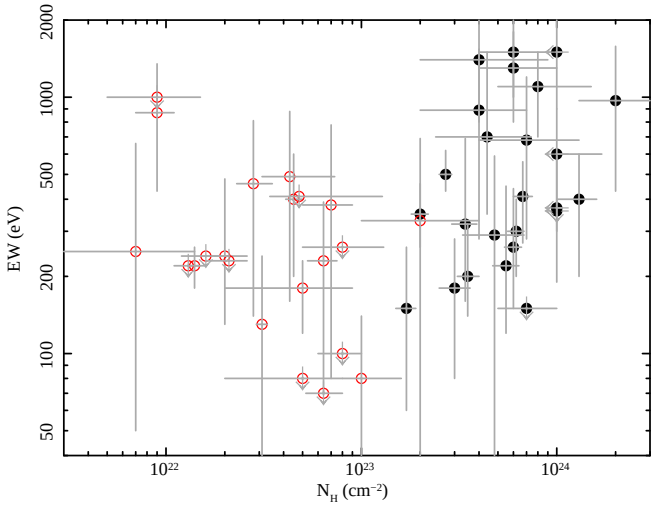

Fig. 7. Column density versus Fe Kα EW for the candidates for which the emission line is detected. Filled circles correspond to the confirmed highly absorbed AGN, empty circles to the remaining AGN.

– 2PL+T+L (`wabs*(zwabs*(pow+zgaus)+mekal+pow)`): same as 2PL+T, plus a narrow emission line defined as in PL+L.
– 2PL+2T+L (`wabs*(zwabs*(pow+zgaus)+mekal+mekal +pow)`): same as 2PL+T+L, plus an additional thermal component.

Of the 81 highly absorbed candidates, **28 sources** display large amounts of absorption in their X-ray spectra. The number of sources that are best-fitted by each of the models described above are listed in Table 1. The manual spectral-fitting results, corresponding to the 28 highly absorbed AGN, are shown in Table 2. In some cases, the addition of ionized absorption (modeled as `absori` in `XSPEC`) is necessary to obtain an acceptable fit. These sources are not considered as highly absorbed in this analysis regardless of the column density of the ionized absorber. In addition, if the resulting scattering fraction in a double power-law model is $\gtrsim$ 10%, we assumed that the model represents partial covering absorption, which means that the soft power-law would correspond to transmitted emission instead of scattered emission. Therefore, these sources were not considered as highly absorbed AGN either, again regardless of the column density of the partial covering absorber. The manually derived column density distribution for the 81 candidates is plotted in Fig. 6, and the column density values versus the Fe Kα line EW values (in the 47 cases in which the line was detected) are plotted in Fig. 7. We find a similar result as reported in Fukazawa et al. (2011). By using *Suzaku*[7] data, the authors reported a positive correlation between the line EW and the measured column density, but only for high column densities.

We considered a source as a CT candidate if the value of N_H was consistent with being higher than 10^{24} cm^{-2}, and/or the value of the Fe Kα line EW was higher than 500 eV. These sources, 15 CT candidates, are marked in boldface in Table 2, and their spectra are plotted in Fig. 8. Only in two cases (3XMMJ131104.6+272806, and 3XMMJ093551.5+612111) were we able to measure a column density higher than 10^{24} cm^{-2}. In four cases (3XMMJ091804.2+514113, 3XMMJ093952.7+355358, 3XMMJ140700.3+282714, and 3XMMJ215649.5-074531), we estimate that the column density is likely higher than 10^{24} cm^{-2} because the X-ray spectrum is reflection dominated, meaning that there is no sign of direct

[7] http://www.isas.jaxa.jp/e/enterp/missions/suzaku/

emission. In five cases, the measured column density is lower than 10^{24} cm^{-2}, but consistent with this value at 90% confidence level. In the remaining four cases, the upper limit at 90% confidence for the column density is lower than 10^{24} cm^{-2}, but these sources display an Fe Kα line with an EW > 500 eV, therefore we also considered them as a CT candidates. A high value of the Fe Kα line EW, along with a very flat hard spectrum, is a characteristic of reflection-dominated spectra. We cannot exclude that the sources displaying high EW values are in fact reflection dominated. However, in all cases, the hard photon indices are either too steep or become steeper if they are left free to vary (in the cases in which the photon index is fixed to 1.9 to constrain the intrinsic absorption), which suggests that the hard emission is direct emission. We finally classified six additional sources as near-CT AGN. These six AGN do not fulfill our CT criteria, but their measured column densities are very high, $N_H \gtrsim 5{\times}10^{23}$ cm^{-2}.

6. Discussion

6.1. Automated selection reliability

The automated selection method presented in this paper can be applied to X-ray spectral data down to 50 source counts. Given the relatively high flux limit of our test sample (typical fluxes are F_X(2-10 keV) $\sim 10^{-13}$ erg cm^{-2} s^{-1}), most of our absorbed sources lie at low redshifts (<z> = 0.15), with the exception of 3XMM141546.2+112943 at z=2.56, which is a lensed QSO, the cloverleaf quasar H1413+117. A much more detailed analysis of this source is presented in Chartas et al. (2007), by using *XMM-Newton* and *Chandra* data, and in which ionized absorption and disk reflection are included in the spectral fit. Since the only limitation to the applicability of this method seems to be the number of collected counts in the X-ray spectra, it could be applied to deeper surveys, and thus, to the selection of highly obscured AGN at higher redshifts.

The fraction of near-CT plus CT candidates (21 AGN with column densities $\gtrsim 5\times 10^{23}$ cm^{-2}) in the FLATH, FLATA, HABS, and HEW samples is 31% (12/67), 12% (4/33), 47% (15/32), and 44% (7/16), respectively. All the sources with manually computed column densities higher than 10^{23} cm^{-2}, including the near-CT, and CT candidates, belong to the FLATH sample. The best selection criterion is a combination of different automated selection criteria. For all sources, regardless of the spectral quality, the best selection criterion is to belong to both the FLATH and the HABS samples (FLATH+HABS subsample), 80% of these sources are absorbed by column densities higher than 10^{23} cm^{-2}. For sources with more than 500 counts, that is, sources for which a selection according to the emission line EW is possible, the best selection criterion is to belong to the HEW and the FLATH samples (FLATH+HEW subsample). Again, 80% of these sources are absorbed by column densities higher than 10^{23} cm^{-2} according to the manual fits. Out of the 28 highly absorbed AGN, 23 belong to either or both of these subsamples.

The sources within the automated selected samples that after the manual spectral fit were found to be not highly absorbed, display one or more of the following spectral characteristics:

- A reflection component, with spectral parameters consistent with those of unabsorbed type 1 AGN, which produces a flat photon index. This feature, combined with a low number of counts at high energies, can also mimic a high EW line.
- Significant amount of absorption, but lower than 10^{23} cm^{-2} (~ several times 10^{22}), totally or partially covering the central source.
- Significant amount of ionized absorption.
- Only in some cases, we found that a low number of counts plus an extremely complex spectral shape classified the source in the HABS sample. The lower number of counts prevented us from using automated complex fits, and the simple power-law fit is an extremely poor fit and returns a high value for the column density.

6.2. Compton-thick candidates and previous results

We searched the literature for previous classifications of our 28 highly absorbed sources and found a very good agreement for most cases. When previously reported intrinsic column density or Fe Kα EW values were available, the source was classified according to our CT candidate definition. In three cases, a previous estimate or measurement of the column density could not be found. Out of the 15 sources that we found to be consistent with being a CT AGN, 12 were previously reported as CT AGN based on different techniques (see Table 3). Our classification disagrees with previous results in only three cases:

- 3XMMJ091804.2+514113: While we classified this source as a reflection-dominated CT candidate, an N_H value of $\sim 6{\times}10^{22}$ is reported in Georgakakis et al. (2006) (although consistent with being highly absorbed within errors). The same XMM-Newton observation was used in both analyses but because there are very few spectral counts, the differences in the spectral-fitting results might be due to the different spectral extraction. Nevertheless, our spectral data display an extremely flat shape that is not consistent with mild absorption.
- 3XMMJ093952.7+355358: If we fit the same best-fit model as in Hardcastle et al. (2006), that is, a double power-law plus an emission line, both best-fit N_H values are consistent within errors, but theirs is lower, probably because the second power-law photon index was left free to vary, which resulted in a very flat slope ($\Gamma \sim 0.5$). Using this model, the source would be also classified as a CT candidate in the current work based solely on the Fe Kα line EW, but we were unable to find the relevant value in Hardcastle et al. (2006). Given the extremely flat hard spectrum, we classify this source as a reflection-dominated CT AGN in this work.
- 3XMMJ122546.7+123943: As for the previous source, the differences between our classification and that reported in Burlon et al. (2011) is caused by the EW of the iron line, which is not reported in Burlon et al. (2011). Moreover, this is a highly variable AGN, and a strong Fe Kα line is only found in one out of the three observations used in this work.

We also searched the literature for CT AGN within our parent sample of 1015 AGN that could have been missed as such by our automated method. Only one AGN from the parent sample is included within the local CT AGN reported in (Brightman & Nandra 2011), NGC 3690, which was classified as a CT AGN because of a high EW Fe Kα emission line. The automated analysis detected an Fe Kα emission line with an EW > 500 eV, but consistent with being lower than that value at the 90% confidence level. Therefore, it was not flagged as

Table 2. Manual spectral-fitting results: Highly absorbed sources with $N_H > 10^{23}$ cm^{-2}

3XMM Name(nobs)	Model	N_H	Γ	S.F.	EW	kT	Flux	Log(Luminosity)	C-stat/d.o.f	Goodness
		10^{22} cm^{-2}		(%)	eV	keV	erg cm^{-2} s^{-1}	erg s^{-1}		(%)
(1)	(2)	(3)	(4)	(5)	(6)	(7)	(8)	(9)	(10)	(11)
3XMMJ080535.0+240950	2PL+T+L	48^{+20}_{-15}	1.9^{f}	2.5	290^{+300}_{-250}	$0.25^{+0.20}_{-0.10}$	2.73×10^{-13}	42.94	195/260	100
3XMMJ080741.0+390015	2PL+T+L	40^{+30}_{-20}	1.9^{f}	6	900^{+700}_{-600}	$0.7^{+0.2}_{-0.2}$	2.15×10^{-13}	41.94	202/209	93
3XMMJ082443.2+295923	2PL+2T+L	20^{+2}_{-2}	$1.9^{+0.2}_{-0.2}$	1	360^{+130}_{-80}	$0.121^{+0.017}_{-0.010}(0.69^{+0.06}_{-0.08})$	1.03×10^{-12}	42.56	1472/1653	100
3XMMJ083139.0+524205(3)	2PL+T+L	30^{+3}_{-3}	$2.3^{+0.2}_{-0.3}$	1	180^{+100}_{-100}	$0.18^{+0.11}_{-0.08}$	7.71×10^{-14}	42.35	1114/1254	100
3XMMJ084002.3+294902	2PL+T+L	62^{+6}_{-6}	1.9^{f}	1	300^{+100}_{-90}	$0.33^{+0.06}_{-0.03}$	7.29×10^{-13}	43.55	1103/1328	100
3XMMJ085331.0+175338	2PL+T	50^{+20}_{-13}	1.9^{f}	2	...	$0.20^{+0.10}_{-0.20}$	1.56×10^{-13}	43.72	189/255	100
3XMMJ091804.2+514113	PL+R+L	>100	1.9^{f}	...	360^{+460}_{-360}	...	7.49×10^{-14}	42.76^{r}	119/120	51
3XMMJ093551.5+612111	2PL+T+L	130^{+30}_{-30}	1.9^{f}	4	400^{+200}_{-200}	$0.7^{+0.4}_{-0.4}$	1.92×10^{-13}	42.88	712/839	100
3XMMJ093952.7+355358	PL+R+L	>100	1.9^{f}	11	370^{+220}_{-180}	...	4.38×10^{-13}	43.26	800/904	100
3XMMJ095906.6+130134	2PL+T+L	17^{+2}_{-2}	$1.9^{+0.3}_{-0.3}$	0.3	150^{+110}_{-90}	$0.44^{+0.15}_{-0.10}$	9.90×10^{-13}	42.82	1081/1273	100
3XMMJ103408.5+600152	2PL+T+L	80^{+70}_{-30}	1.9^{f}	9	1100^{+400}_{-400}	$0.19^{+0.02}_{-0.02}$	1.99×10^{-13}	42.75	560/533	66
3XMMJ104930.9+225752	2PL+T+L	55^{+8}_{-7}	$1.5^{+0.3}_{-0.3}$	2	220^{+170}_{-100}	$0.18^{+0.02}_{-0.04}$	1.59×10^{-12}	43.17	895/1025	100
3XMMJ113240.2+525701(2)	2PL+T+L	60^{+7}_{-6}	$2.28^{+0.13}_{-0.13}$	0.3	410^{+150}_{-140}	$0.66^{+0.09}_{-0.06}$	4.72×10^{-13}	42.69	863/985	100
3XMMJ113549.0+565708	2PL+T+L	70^{+60}_{-30}	$2.84^{+0.13}_{-0.13}$	3	700^{+500}_{-400}	$0.8^{+0.2}_{-0.2}$	5.22×10^{-14}	42.43	515/514	83
3XMMJ114454.8+194635	2PL	29^{+20}_{-11}	$1.7^{+0.3}_{-0.3}$	11	...	...	6.72×10^{-14}	41.44	394/428	99
3XMMJ115704.8+524903	2PL+T+L	60^{+40}_{-20}	$2.6^{+0.2}_{-0.2}$	3	1500^{+500}_{-500}	$0.20^{+0.03}_{-0.02}$	9.26×10^{-14}	42.18	634/617	74
3XMMJ120429.6+201858(2)	2PL+T+L	34^{+5}_{-5}	$1.8^{+0.4}_{-0.4}$	1	320^{+370}_{-160}	$0.14^{+0.06}_{-0.05}$	1.73×10^{-12}	42.81	416/477	100
3XMMJ120429.6+201858(1)	2PL+T+L	22^{+3}_{-3}	1.8^{f}	1	320^{+200}_{-170}	$0.25^{+0.20}_{-0.10}$	2.98×10^{-12}	42.93	293/332	100
3XMMJ121839.4+470626(2)	2PL+T+L	44^{+30}_{-20}	$2.2^{+0.3}_{-0.4}$	4	700^{+800}_{-350}	$0.14^{+0.04}_{-0.04}$	7.95×10^{-14}	42.80	412/420	89
3XMMJ122546.7+123943(1)	2PL+T+L	27^{+2}_{-2}	$1.4^{+0.2}_{-0.2}$	3	500^{+120}_{-70}	$0.27^{+0.03}_{-0.02}$	7.44×10^{-12}	42.45	1896/2106	100
3XMMJ122546.7+123943(1)	2PL+T+L	$28.7^{+1.1}_{-1.1}$	$1.52^{+0.09}_{-0.09}$	0.7	220^{+30}_{-20}	$0.27^{+0.03}_{-0.01}$	2.11×10^{-11}	42.96	2879/2801	92
3XMMJ122546.7+123943(1)	2PL+T+L	$23.6^{+0.4}_{-0.4}$	$1.59^{+0.03}_{-0.04}$	0.3	90^{+10}_{-10}	$0.30^{+0.01}_{-0.01}$	4.13×10^{-11}	43.23	4268/3129	0
3XMMJ123843.4+092736	2PL+2T+L	35^{+5}_{-4}	$1.5^{+0.3}_{-0.2}$	2	180^{+120}_{-60}	$0.15^{+0.02}_{-0.02}(0.70^{+0.07}_{-0.09})$	1.11×10^{-12}	43.69	1530/1618	100
3XMMJ131104.6+272806	2PL+T+L	200^{+120}_{-70}	1.9^{f}	3	970^{+610}_{-540}	$0.19^{+0.05}_{-0.05}$	3.40×10^{-14}	43.80	398/446	100
3XMMJ132348.4+431804	2PL+T+L	60^{+6}_{-6}	$2.4^{+0.3}_{-0.2}$	0.2	260^{+200}_{-110}	$0.7^{+0.5}_{-0.3}$	8.70×10^{-13}	43.02	790/971	100
3XMMJ140700.3+282714	PL+R+L	>100	1.9^{f}	...	600^{+300}_{-300}	...	2.85×10^{-13}	42.58^{r}	646/808	100
3XMMJ141546.2+112943(2)	2PL+L	70^{+30}_{-20}	1.9^{f}	4	150^{+120}_{-150}	...	5.97×10^{-14}	45.61	302/365	100
3XMMJ150754.3+010817	2PL+T+L	60^{+40}_{-20}	1.9^{f}	5	1300^{+500}_{-500}	$0.15^{+0.03}_{-0.04}$	1.12×10^{-13}	42.61	392/426	99
3XMMJ150946.8+570002	2PL+T	23^{+20}_{-11}	1.9^{f}	3	...	$0.34^{+0.20}_{-0.07}$	1.36×10^{-13}	39.72	118/124	83
3XMMJ153457.2+233011(4)	PL+T+R+L	>100	1.9^{f}	...	1500^{+800}_{-600}	$0.9^{+0.4}_{-0.3}$	1.11×10^{-13}	40.92^{r}	556/610	100
3XMMJ215649.5-074531(2)	2PL+T+L	40^{+50}_{-20}	1.9^{f}	9	1400^{+700}_{-600}	$0.20^{+0.04}_{-0.02}$	4.80×10^{-14}	41.99	461/463	75

Notes. *Columns:* (1) Source name in the 3XMM-DR4 catalog. (2) Best-fit model. (3) Intrinsic column density. (4) Power-law photon index. (5) Scattered fraction in the double power-law model (ratio between the power-law normalizations). (6) Equivalent width of the Fe Kα emission line. (7) Plasma temperature in the thermal model. (8) Observed flux in 2-10 keV. (9) Intrinsic luminosity in 2-10 keV. (10) C-stat likelihood value over degrees of freedom. (11) Goodness of fit estimated as 100-`XSPEC goodness`. Numbers between parenthesis after the name of the source correspond to the number of merged observations. Compton-thick candidates are in boldface. $^{(f)}$ Fixed parameter. $^{(r)}$ No direct continuum.

Table 3. Candidate Compton-thick AGN

Name in 3XMM-DR4	Other names	Redshift	Previous classification	Reference
3XMMJ080741.0+390015	UGC 4229	0.0234	CT?	1
3XMMJ091804.2+514113	SDSS J091804.19+514113.5	0.186	ABS	2
3XMMJ093551.5+612111	UGC 5101	0.0393	CT	3
3XMMJ093952.7+355358	3C 223	0.1367	ABS	4
3XMMJ103408.5+600152	Mrk 34	0.051	CT	5
3XMMJ113549.0+565708	SBS 1133+572	0.0511	CT?	6
3XMMJ115704.8+524903	2MASX J11570483+5299036	0.0355	CT	6
3XMMJ121839.4+470626	2MASX J12183945+4706275	0.0939	CT?	6
3XMMJ122546.7+123943	NGC 4388	0.00856	HABS	7
3XMMJ131104.6+272806	3C 284	0.2397	CT	4
3XMMJ140700.3+282714	Mrk 668	0.0766	CT	8
3XMMJ141546.2+112943	H1413+117	2.5603	CT	9
3XMMJ150754.3+010817	2MASX J15075440+0108168	0.061	CT?	10
3XMMJ153457.2+233011	Arp 220	0.01814	CT?	3
3XMMJ215649.5-074531	2MASX J21564950-0745325	0.0554	CT	11

Notes. Previous classification: ABS: 10^{22} cm^{-2} <N_H <10^{23} cm^{-2}; HABS: N_H >10^{23} cm^{-2}; CT(?): Compton-thick (candidate).

References. (1) Guainazzi et al. (2005); (2) Georgakakis et al. (2006); (3) Severgnini et al. (2012); (4) Hardcastle et al. (2006); (5) Greenhill et al. (2008); (6) LaMassa et al. (2009); (7) Burlon et al. (2011); (8) Guainazzi et al. (2004); (9) Chartas et al. (2007); (10) Lewis et al. (2011); (11) Goulding et al. (2011).

a highly absorbed candidate by our selection criteria. Of the sources in out parent sample that are classified as CT AGN within the sample of type 2 Seyfert galaxies extracted from the SDSS presented in LaMassa et al. (2009), our classification agrees in all but two cases: SDSS J080359.20+234520.4, and SDSS J112301.31+470308.6. In both cases, the automated fits return very flat photon indices in the hard band, but because of the very low number of counts in that band, consistent with being larger than 1.4 at the 90% confidence level. As a result, these two sources are not flagged as candidates by our selection criteria. It is important to note that these two sources are classified as CT AGN in LaMassa et al. (2009) based on their X-ray luminosity to optical, and mid-IR luminosity ratios, and not from their X-ray spectral analysis. Finally, we cross-correlated our parent sample with the CT AGN within the two type 2 QSO samples that were also extracted from the SDSS and reported in Vignali et al. (2010), and Jia et al. (2013). Our classification agrees with that in those works except in one case: SDSS J091345.48+405628.2. Nevertheless, as pointed out in Jia et al. (2013), its X-ray spectrum is complex and dominated by soft emission, and in addition, different X-ray spectral analysis of this source, both using *XMM-Newton* and *Chandra* data, have been published reporting a non-CT classification in some cases.

6.3. Hardness ratios versus automated spectral-fit selection

Rest-frame hardness ratios (or X-ray colors) have been proposed by several other studies as an alternative to manual spectral fitting for the selection of highly absorbed sources. The downside of these methods is that to obtain rest-frame colors (or fluxes) from X-ray count rates, a spectral model has to be assumed. This could strongly decrease the accuracy of the selection technique, especially if the assumed spectral model is a poor representation of the actual spectral shape. To compare our proposed technique with color-selection techniques, X-ray colors were computed for our sample following the two different X-ray color selection techniques presented in Brightman & Nandra (2012) and Iwasawa et al. (2012).

Brightman & Nandra (2012) presented an X-ray color selection calibrated by using rest-frame fluxes derived from best-fit models and manual spectral fits. To this end, they used *XMM-Newton* spectra for a sample of 126 local AGN, extracted from a parent sample selected in the mid-IR, for which they carried out a detailed X-ray spectral analysis. Brightman & Nandra (2012) defined two X-ray colors, HR1 and HR2, based on rest-frame fluxes computed in the rest frame bands: 1-2 keV (band 1), 2-4 keV (band 2), and 4-16 keV (band 3), as follows:

$$\mathrm{HR1} = \frac{\mathrm{F(band2)-F(band1)}}{\mathrm{F(band2)+F(band1)}} \qquad \mathrm{HR1} = \frac{\mathrm{F(band3)-F(band2)}}{\mathrm{F(band3)+F(band2)}} \quad . \tag{1}$$

First, we applied this method to our sample of 81 highly absorbed candidates by using the best-fit model obtained from the manual fits. The results are plotted in Fig. 9 in the top-left panel. The dashed line corresponds to the proposed dividing line between highly absorbed sources ($N_H > 10^{23}$ cm^{-2}) and mildly absorbed or unabsorbed sources in Brightman & Nandra (2012). The solid line corresponds to the wedge defined in that work to contain all their CT AGN. We found similar results, that is, all highly absorbed sources in our sample but one lie above the dashed line. Nevertheless, we found a higher number of contaminants with lower N_H of ~ 20%, while a value of only 7% was reported in Brightman & Nandra (2012). Moreover, not all our CT candidates fall within the solid wedge.

Brightman & Nandra (2012) also proposed that their selection technique could be applied to X-ray colors derived by using observed count rates, assuming a simple power-law model (Γ = 1.4), and using the HEASARC portable interactive multimission software (PIMMS) to derive the rest-frame fluxes. However, when we applied that method to obtain the X-ray colors (Fig. 9: top-right panel), the contamination of the highly absorbed region by sources with lower N_H increases dramatically. As a comparison, we derived the X-ray colors by using the best-fit model from the automated spectral fits (Fig. 9: bottom-left panel). We found a lower contamination of the highly absorbed

AGN area by unabsorbed AGN, but still quite high.

As a final step, we derived X-ray colors by using automated fits for the sources in the full sample that were not flagged as highly absorbed candidates by the automated selection (Fig. 9: bottom-right panel) to check whether we might be missing a significant number of highly absorbed AGN. We found that only 10% of the not selected sources lie above the dashed line. In Brightman & Nandra (2012), most of the low N_H contaminants of that region were sources with a complex spectrum. In our case, since manual fit results are not available for the full sample, we checked for the best-fit automated model for these sources. In 95% of the cases, the preferred model was in fact a complex one. Therefore, these sources are probably not highly absorbed sources missed by our selection criteria, but sources showing a complex X-ray spectrum.

Iwasawa et al. (2012) presented a different method based on observed count rates instead of rest-frame fluxes, and designed to efficiently select highly absorbed sources at redshifts higher than 1.7. The sample used to test this method was composed of 47 AGN detected at high significance in the XMM-CDFS, and with either photometric or spectroscopic redshifts available. They also compared their results with those obtained by using high-energy data (> 10 keV) for a very small sample of local and well-known AGN. The method presented in Iwasawa et al. (2012) is based on the use of observed count rates in the following rest-frame energy bands: 3-5 keV (band s), 5-9 keV (band m), and 9-20 keV (band h). They defined two colors as s/m and h/m. Since most of our highly absorbed candidates are at low redshift, these three energy bands are not covered by most of our *XMM-Newton* data. To be able to apply a method as similar to that in Iwasawa et al. (2012) as possible, we used rest-frame fluxes instead of count rates. As for the X-ray colors in Brightman & Nandra (2012), a model has to be assumed to obtain the s/m and h/m colors in this case.

We performed the same comparison as for the colors in Brightman & Nandra (2012). The results are plotted in Fig. 10. First, we used the best-fit model from the manual fits to recover the X-ray colors (Fig. 10: top-left panel). The dashed lines limit the different regions according to the expected column densities. Regions U (unabsorbed), M (modestly absorbed), A (absorbed), and V (very absorbed) correspond to sources with typical log N_H lower than 22, 22.7, 23.4, and 23.8, respectively. We drew a tentative limit (solid line) that separates sources with $N_H > 10^{23}$cm^{-2} in our sample. This method very efficiently separates moderate or unabsorbed AGN from highly absorbed AGN. However, as for the Brightman & Nandra (2012), and the automated selection criteria, we cannot separate highly absorbed sources from CT candidates. We repeated the same exercise by using PIMMS (assuming a power-law model with photon index equal to 1.4, Fig. 10: top-right panel), and by using the automated spectral-fitting results (Fig. 10: bottom-left panel). The contamination of low N_H sources is similar in both cases. In the automated fits, highly obscured AGN occupy a broader region of the plot, while for PIMMS colors, the highly obscured region is contaminated by unabsorbed AGN. The method of Iwasawa et al. (2012) seems to separate AGN with different amounts of intrinsic absorption much better than that presented in Brightman & Nandra (2012).

Finally, we applied this method to the full sample by using the best-fit model from the automated fits (Fig. 10: bottom-right panel). All the sources not classified as highly absorbed candidates by our automated criteria fall outside the highly absorbed AGN region.

7. Conclusions

We have derived X-ray spectral fits for very many 3XMM-DR4 sources (∼ 77 000) that contain more than 50 photons per detector (Corral et al. 2014). Here, we used a subsample of ≃ 1000 AGN in the common SDSS and 3XMM area (covering 120 deg^2) with spectroscopic redshifts available. We searched for highly obscured AGN by applying an automated selection technique based on an automated X-ray spectral analysis. In particular, the selection was based on the presence of a) flat spectra with a photon index lower than 1.4 at the 90% confidence level in the 2-10 keV rest-frame spectra, b) flat spectra with a photon index lower than 1.4 at the 90% confidence level in the 0.5-10 keV observed spectra, c) an absorption turnover, indicative of a high rest-frame column density, or d) an Fe Kα line with a large equivalent width (>500 eV). We found 81 candidate highly obscured sources. Subsequent detailed manual spectral fits revealed that 28 are heavily obscured with a column density of $N_H > 10^{23}$ cm^{-2}. Of these 28 sources, six are near-CT AGN with a column density of $N_H \sim 5\times 10^{23}$ cm^{-2}. Finally, 15 are candidate CT AGN on the basis of either a high column density, consistent within the 90% confidence level with 10^{24} cm^{-2}, or a large equivalent width (>500 eV) of the Fe Kα line.

Our automated method is very efficient in selecting highly absorbed AGN ($N_H > 10^{23}$ cm^{-2}), with a successful rate of 80%:

- For low-quality spectra, and by using only results from a simple absorbed power-law fit, 80% (20 out of 25 AGN) of the sources whose X-ray spectra were flagged as flat in the 2-10 rest-frame band and for which the automatically derived column density was higher than 5×10^{23} cm^{-2} were highly absorbed, as tested by using manual spectral fits.
- For medium- to high-quality spectra, 80% (7 out of 9 AGN) of the sources with an automatically detected high EW Fe Kα line, plus a flat continuum in the 2-10 keV rest frame band were highly absorbed, as tested by using manual spectral fits.

We compared our results with rest-frame color CT AGN selection techniques developed by Brightman & Nandra (2012) and Iwasawa et al. (2012). The method of Iwasawa et al. (2012), modified by using a spectral model to obtain rest-frame fluxes, was the best for separating highly absorbed ($N_H > 10^{23}$ cm^{-2}) from moderately to unabsorbed sources.

Acknowledgements. Based on observations obtained with *XMM-Newton*, an ESA science mission with instruments and contributions directly funded by ESA Member States and NASA. A. Corral acknowledges financial support by the European Space Agency (ESA) under the PRODEX program. P. Ranalli and E. Koulouridis acknowledge financial support from the 'Support to Postdoctoral Researchers' projects PE9-3493 and PE9-1145 which are jointly funded by the European Union and the Greek Government in the framework of the programme *Education and lifelong learning*. G. Mountrichas and G. Lanzuisi acknowledge financial support from the THALES project 383549, which is jointly funded by the European Union and the Greek Government in the framework of the programme *Education and lifelong learning*. We thank the referee for providing constructive comments and suggestions that helped to improve this paper.

References

Akylas, A., Georgakakis, A., Georgantopoulos, I., Brightman, M., & Nandra, K. 2012, A&A, 546, A98

Akylas, A., Georgantopoulos, I., Georgakakis, A., Kitsionas, S., & Hatziminaoglou, E. 2006, A&A, 459, 693
Alexander, D. M., Stern, D., Del Moro, A., et al. 2013, ApJ, 773, 125
Arnaud, K. A. 1996, in Astronomical Society of the Pacific Conference Series, Vol. 101, Astronomical Data Analysis Software and Systems V, ed. G. H. Jacoby & J. Barnes, 17
Ballantyne, D. R., Draper, A. R., Madsen, K. K., Rigby, J. R., & Treister, E. 2011, ApJ, 736, 56
Barmby, P., Alonso-Herrero, A., Donley, J. L., et al. 2006, ApJ, 642, 126
Bongiorno, A., Mignoli, M., Zamorani, G., et al. 2010, A&A, 510, A56
Brightman, M. & Nandra, K. 2011, MNRAS, 413, 1206
Brightman, M. & Nandra, K. 2012, MNRAS, 422, 1166
Brightman, M. & Ueda, Y. 2012, MNRAS, 423, 702
Brown, M. J. I., Brand, K., Dey, A., et al. 2006, ApJ, 638, 88
Burlon, D., Ajello, M., Greiner, J., et al. 2011, ApJ, 728, 58
Chartas, G., Eracleous, M., Dai, X., Agol, E., & Gallagher, S. 2007, ApJ, 661, 678
Comastri, A., Ranalli, P., Iwasawa, K., et al. 2011, A&A, 526, L9
Corral, A., Georgantopoulos, I., Rosen, S., et al. 2014, arXiv:1402.3041
Delvecchio, I., Gruppioni, C., Pozzi, F., et al. 2014, MNRAS, 439, 2736
Frontera, F., Orlandini, M., Landi, R., et al. 2007, ApJ, 666, 86
Fukazawa, Y., Hiragi, K., Mizuno, M., et al. 2011, ApJ, 727, 19
Georgakakis, A. & Nandra, K. 2011, MNRAS, 414, 992
Georgakakis, A. E., Georgantopoulos, I., & Akylas, A. 2006, MNRAS, 366, 171
Georgantopoulos, I., Comastri, A., Vignali, C., et al. 2013, A&A, 555, A43
Georgantopoulos, I., Georgakakis, A., Rowan-Robinson, M., & Rovilos, E. 2008, A&A, 484, 671
Gilli, R., Comastri, A., & Hasinger, G. 2007, A&A, 463, 79
Goulding, A. D., Alexander, D. M., Mullaney, J. R., et al. 2011, MNRAS, 411, 1231
Greenhill, L. J., Tilak, A., & Madejski, G. 2008, ApJ, 686, L13
Guainazzi, M., Matt, G., & Perola, G. C. 2005, A&A, 444, 119
Guainazzi, M., Siemiginowska, A., Rodriguez-Pascual, P., & Stanghellini, C. 2004, A&A, 421, 461
Hardcastle, M. J., Evans, D. A., & Croston, J. H. 2006, MNRAS, 370, 1893
Iwasawa, K., Gilli, R., Vignali, C., et al. 2012, A&A, 546, A84
Jia, J., Ptak, A., Heckman, T., & Zakamska, N. L. 2013, ApJ, 777, 27
Krumpe, M., Lamer, G., Corral, A., et al. 2008, A&A, 483, 415
LaMassa, S. M., Heckman, T. M., Ptak, A., et al. 2009, ApJ, 705, 568
Lansbury, G. B., Alexander, D. M., Del Moro, A., et al. 2014, ArXiv e-prints
Lewis, K. T., Sambruna, R. M., Angelakis, E., et al. 2011, AJ, 142, 9
Moretti, A., Pagani, C., Cusumano, G., et al. 2009, A&A, 493, 501
Severgnini, P., Caccianiga, A., & Della Ceca, R. 2012, A&A, 542, A46
Tozzi, P., Gilli, R., Mainieri, V., et al. 2006, A&A, 451, 457
Treister, E., Urry, C. M., & Virani, S. 2009, ApJ, 696, 110
Vignali, C., Alexander, D. M., Gilli, R., & Pozzi, F. 2010, MNRAS, 404, 48
Watson, M. G., Schröder, A. C., Fyfe, D., et al. 2009, A&A, 493, 339
Xue, Y. Q., Luo, B., Brandt, W. N., et al. 2011, ApJS, 195, 10

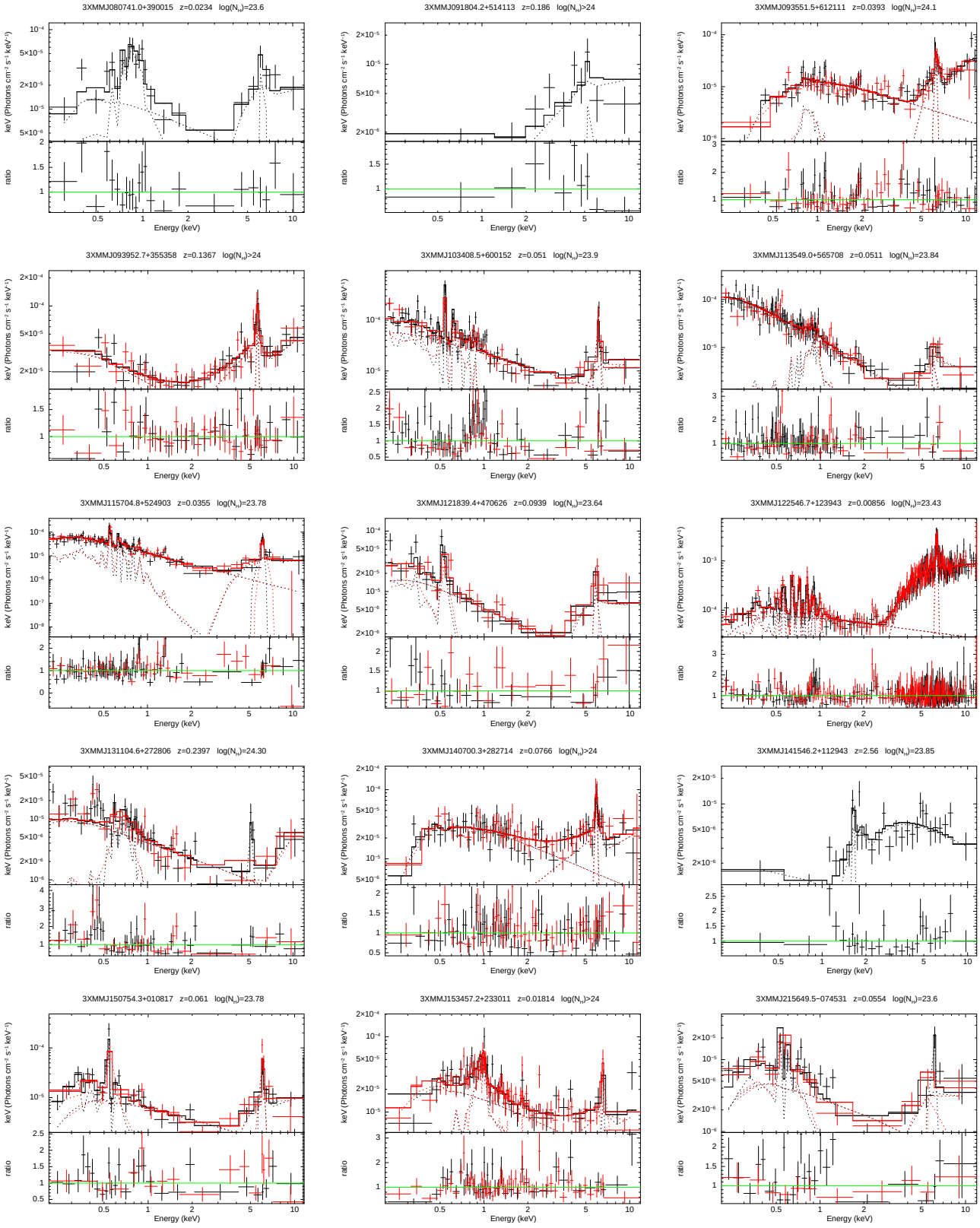

Fig. 8. Unfolded spectra and model, and data to model ratio for the Compton-thick candidates.

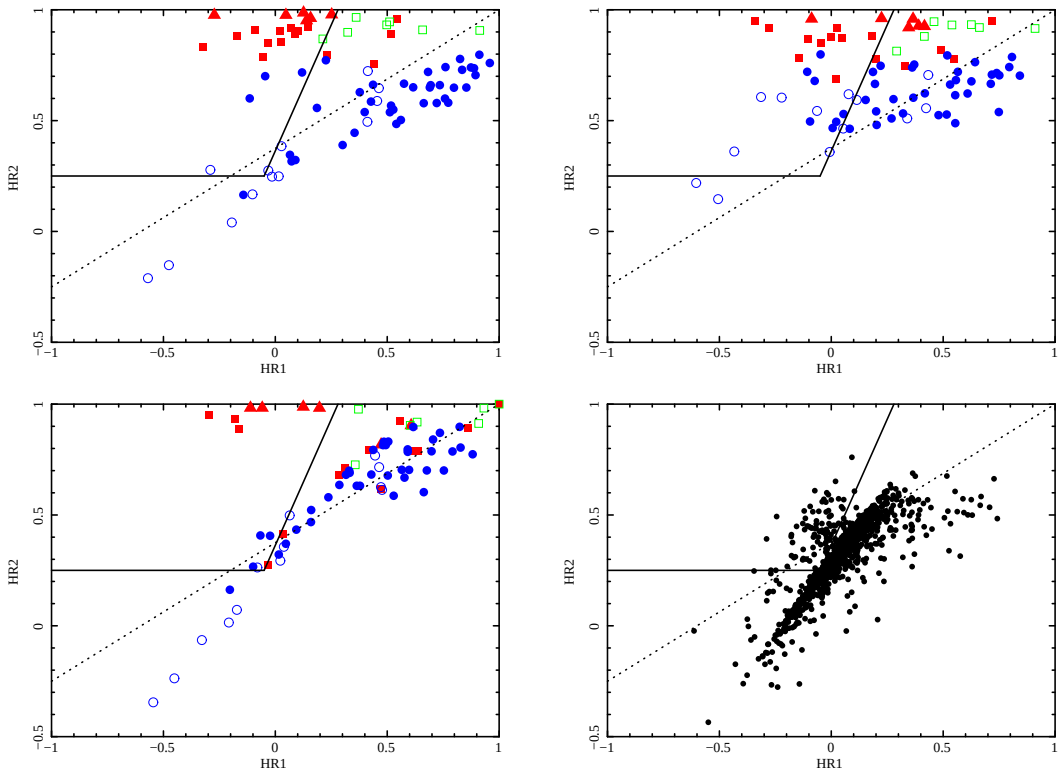

Fig. 9. X-ray colors as in Brightman & Nandra (2012). Different symbols correspond to column densities from manual spectral fits: CT candidate (filled squares), near-CT (filled triangles), $\log(N_H) > 23$ (empty squares), $22 < \log(N_H) < 23$ (filled circles), and $\log(N_H) < 22$ (empty circles). Top-left: X-ray colors derived from manual spectral analysis. Top-right: colors obtained by using HEASARC PIMMS (see text for details). Bottom-left: colors obtained by using automated spectral fits. Bottom-right: colors obtained by using automated spectral fits for the sources not belonging to the sample of highly absorbed candidates.

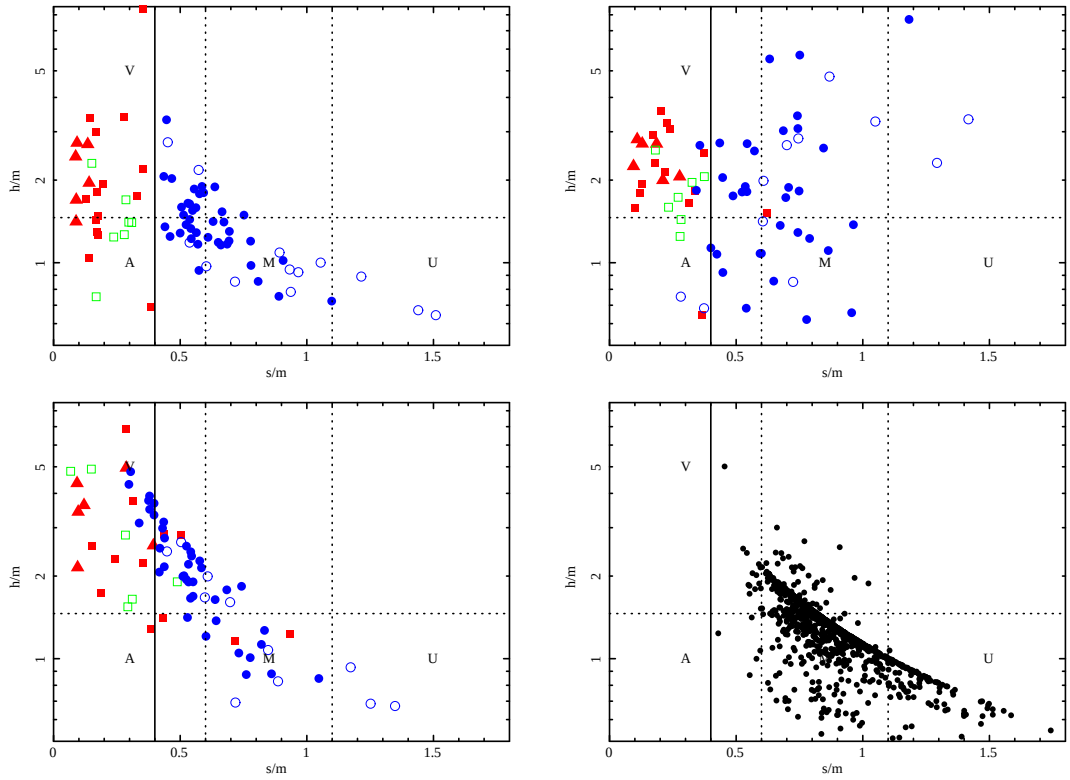

Fig. 10. X-ray colors as in Iwasawa et al. (2012). Different symbols correspond to column densities from manual spectral fits: CT candidate (filled squares), near-CT (filled triangles), log(N_H) > 23 (empty squares), 22 < log(N_H) < 23 (filled circles), and log(N_H) < 22 (empty circles). Top-left: X-ray colors derived from manual spectral analysis. Top-right: colors obtained by using HEASARC PIMMS (see text for details). Bottom-left: colors obtained by using automated spectral fits. Bottom-right: colors obtained by using automated spectral fits for the sources not belonging to the sample of highly absorbed candidates.

Table 4. Sample of highly absorbed candidates.

3XMM Name (1)	Redshift (2)	Observation (3)	Counts (4)	HEW (5)	FLATH (6)	HABS (7)	FLATA (8)	CAND (9)
3XMMJ021047.0-100153	0.5401	0204340201	162	N	Y	N	Y	Y
3XMMJ073534.9+435414	0.1918	0083000101	245	N	Y	Y	N	Y
3XMMJ080020.9+263648	0.0268	0504101201	17553	N	Y	N	Y	Y
3XMMJ080535.0+240950	0.0597	0203280201	220	N	Y	Y	N	Y
3XMMJ080741.0+390015	0.0234	0138951401	217	N	Y	Y	N	Y
3XMMJ082035.6+210404	0.0151	0505930301	4685	Y	N	N	N	Y
		0108860501	3131	N	N	N	N	N
3XMMJ082443.2+295923	0.0253	0504102001	3224	N	Y	Y	N	Y
3XMMJ083139.0+524205	0.0585	0092800201	654	N	Y	N	Y	Y
		0502220201	325	N	Y	N	Y	Y
		0502220301	475	N	Y	N	Y	Y
3XMMJ083924.9+575231	0.187	0406541201	142	N	N	N	N	N
		0406541001	64	N	N	N	N	N
		0406540201	758	Y	N	N	N	Y
3XMMJ084002.3+294902	0.0648	0504120101	2088	N	Y	Y	N	Y
3XMMJ085331.0+175338	0.1866	0305480301	189	N	Y	Y	N	Y
3XMMJ091127.5+055053	2.7633	0083240201	791	N	Y	N	N	Y
3XMMJ091804.2+514113	0.186	0084230601	77	N	Y	N	N	Y
3XMMJ091828.5+513929	0.1855	0084230601	395	N	Y	N	Y	Y
3XMMJ092718.3+304538	0.5267	0200730101	126	N	N	Y	N	Y
3XMMJ093255.4+284038	0.5468	0304071301	480	N	Y	Y	N	Y
3XMMJ093458.3+611233	0.245	0085640201	391	N	Y	N	Y	Y
3XMMJ093532.9+612739	0.4755	0085640201	112	N	Y	N	Y	Y
3XMMJ093551.5+612111	0.0393	0085640201	1028	Y	Y	N	Y	Y
3XMMJ093952.7+355358	0.1367	0021740101	1195	Y	Y	Y	N	Y
3XMMJ095902.7+021906	0.3454	0203362301	1046	N	N	N	N	N
		0203362201	2459	N	N	N	N	N
		0203361801	2851	N	N	N	N	N
		0302351801	1088	N	N	N	N	N
		0501170201	1208	N	N	Y	N	Y
		0302351701	688	N	N	N	N	N
		0302352301	110	N	N	N	N	N
		0302352201	282	N	N	N	N	N
		0203361701	1150	N	N	N	N	N
3XMMJ095906.6+130134	0.0366	0504100201	1937	N	Y	Y	N	Y
3XMMJ100032.2+553630	0.215	0110930201	246	N	N	Y	N	Y
		0147760101	227	N	Y	N	N	Y
3XMMJ100129.4+013633	0.1042	0203360501	152	N	Y	N	Y	Y
		0302351001	553	N	Y	N	N	Y
		0203361001	516	N	Y	N	N	Y
3XMMJ101830.8+000504	0.0623	0402781401	1587	N	Y	N	N	Y
		0402780101	668	N	Y	N	N	Y

Table 4. continued.

3XMM Name (1)	Redshift (2)	Observation (3)	Counts (4)	HEW (5)	FLATH (6)	HABS (7)	FLATA (8)	CAND (9)
3XMMJ103408.5+600152	0.051	0306050701	745	Y	Y	Y	N	Y
3XMMJ104451.7+063548	0.0276	0405240901	1275	Y	N	N	N	Y
3XMMJ104522.1+212614	0.8908	0128531601	4732	N	N	N	N	N
		0128531501	921	N	N	N	N	N
		0128531401	571	N	Y	N	Y	Y
3XMMJ104930.9+225752	0.0327	0312191501	1260	N	Y	Y	N	Y
3XMMJ111217.9+132106	0.2315	0500760101	299	N	N	Y	N	Y
3XMMJ112026.6+431518	0.1459	0107860201	184	N	Y	N	Y	Y
3XMMJ112345.1+061605	0.2338	0103863201	269	N	N	Y	N	Y
3XMMJ113240.2+525701	0.0266	0200431301	620	N	Y	Y	N	Y
		0200430501	919	N	Y	Y	N	Y
3XMMJ113409.0+491516	0.0372	0149900201	1170	N	Y	N	N	Y
3XMMJ113549.0+565708	0.0511	0504101001	697	N	Y	Y	N	Y
3XMMJ114209.9+600435	0.3477	0502780301	988	Y	N	N	N	Y
3XMMJ114454.8+194635	0.0274	0061740101	196	N	Y	N	Y	Y
3XMMJ115704.8+524903	0.0355	0504100901	885	Y	Y	Y	N	Y
3XMMJ120349.1+020556	0.081	0093060101	371	N	Y	N	Y	Y
3XMMJ120429.6+201858	0.0226	0112271001	260	N	Y	Y	N	Y
		0112271101	381	N	Y	Y	N	Y
		0112270601	555	N	Y	N	N	Y
3XMMJ120629.3+281435	0.2927	0301900401	99	N	Y	N	Y	Y
3XMMJ121118.8+503652	0.1023	0203170101	4145	N	Y	N	Y	Y
3XMMJ121839.4+470626	0.0939	0203270201	188	N	Y	Y	N	Y
		0400560301	158	N	Y	Y	N	Y
3XMMJ121923.2+054929	0.0073	0502120101	46994	Y	Y	N	N	Y
		0056340101	16369	N	Y	N	N	Y
3XMMJ122135.6+280614	3.2877	0502211101	203	N	N	N	N	N
		0502211301	465	N	N	N	N	N
		0502211401	168	N	N	N	N	N
		0104860501	4615	N	Y	N	Y	Y
		0502211201	137	N	N	N	N	N
3XMMJ122349.5+072657	0.0013	0205090101	1130	Y	N	N	N	Y
3XMMJ122546.7+123943	0.0086	0110930301	5250	N	Y	N	Y	Y
		0110930701	19165	N	Y	Y	N	Y
		0675140101	116555	Y	Y	N	N	Y
3XMMJ122548.8+333248	0.001	0112522001	2062	N	Y	Y	N	Y
		0142830101	145167	N	Y	N	Y	Y
		0112522701	11519	N	Y	N	Y	Y
		0112521901	10640	N	Y	Y	N	Y
3XMMJ123056.2+155212	0.1877	0106061001	200	N	Y	N	Y	Y
3XMMJ123625.4+125843	0.0934	0200650101	1313	N	Y	N	N	Y
3XMMJ123719.3+114915	0.1075	0112840101	101	N	Y	N	Y	Y

Table 4. continued.

3XMM Name (1)	Redshift (2)	Observation (3)	Counts (4)	HEW (5)	FLATH (6)	HABS (7)	FLATA (8)	CAND (9)
3XMMJ123843.4+092736	0.0829	0504100601	2876	N	Y	Y	N	Y
3XMMJ125710.7+272417	0.0207	0652310401	1060	N	N	N	N	N
		0652310501	79	N	N	N	N	N
		0652310301	295	N	N	N	N	N
		0652310601	61	N	N	N	N	N
		0403150201	606	N	N	N	Y	Y
		0652310701	986	N	N	N	N	N
		0124710101	1277	N	N	N	N	N
		0652311001	744	Y	N	N	N	Y
		0403150101	288	N	Y	N	Y	Y
		0652310901	1763	N	N	N	N	N
		0652310201	724	N	N	N	N	N
		0652310801	714	N	N	N	N	N
3XMMJ125724.3+272952	0.0245	0124712201	213	N	N	N	N	N
		0652310601	187	N	N	N	N	N
		0652311001	156	N	N	N	N	N
		0652310901	509	N	N	N	N	N
		0652310801	448	N	N	N	N	N
		0652310201	277	N	N	N	N	N
		0652310701	449	N	N	N	N	N
		0124710101	991	Y	N	N	N	Y
		0403150201	1288	N	N	N	N	N
		0403150101	978	N	N	N	N	N
		0652310401	769	N	N	N	N	N
3XMMJ125930.9+282705	1.0939	0204040301	109	N	N	N	N	N
		0204040201	216	N	Y	N	N	Y
		0204040101	514	N	Y	N	Y	Y
		0304320201	154	N	N	N	Y	Y
3XMMJ130128.1+275106	0.2425	0124710901	886	Y	N	N	N	Y
		0124710801	1308	N	N	N	N	N
3XMMJ131104.6+272806	0.2397	0021740201	423	N	Y	N	N	Y
3XMMJ132348.4+431804	0.0273	0504101601	1149	N	Y	Y	N	Y
3XMMJ132410.0+135835	0.023	0108860701	3164	Y	N	N	N	Y
3XMMJ133807.5+280508	1.0881	0110940101	567	N	Y	N	Y	Y
3XMMJ134245.8+403913	0.0893	0070340701	857	N	Y	Y	N	Y
3XMMJ134459.4-001559	0.2449	0111282501	507	N	N	Y	N	Y
		0111281801	625	N	N	N	N	N
3XMMJ134507.9-001900	0.4189	0111282501	363	N	Y	N	N	Y
3XMMJ134656.6+580316	0.3722	0112250201	188	N	Y	N	Y	Y
3XMMJ134745.6+264053	0.2529	0205190101	460	N	N	Y	N	Y
3XMMJ134834.9+263109	0.0589	0109070201	20801	Y	N	N	N	Y
		0097820101	49559	N	N	N	N	N
3XMMJ135436.3+051524	0.0815	0404240101	272	N	Y	N	Y	Y

Table 4. continued.

3XMM Name (1)	Redshift (2)	Observation (3)	Counts (4)	HEW (5)	FLATH (6)	HABS (7)	FLATA (8)	CAND (9)
3XMMJ140040.5-015518	0.025	0200430901	132	N	N	N	N	N
		0505930101	110	N	N	N	N	N
		0505930401	115	N	N	Y	Y	Y
3XMMJ140700.3+282714	0.0766	0140960101	1110	Y	Y	N	Y	Y
3XMMJ141546.2+112943	2.5603	0112250301	156	N	Y	N	Y	Y
		0112251301	163	N	Y	N	Y	Y
3XMMJ141602.1+360923	0.171	0148620101	569	N	Y	N	N	Y
3XMMJ143025.8+415956	0.3524	0212480701	430	N	Y	N	Y	Y
		0111260101	345	N	N	N	N	N
		0111260701	1458	N	N	N	N	N
3XMMJ144659.9+025330	0.0013	0203050401	1072	N	Y	N	Y	Y
		0203050801	3488	N	Y	N	Y	Y
3XMMJ145301.4+164452	0.8386	0091140201	352	N	Y	N	Y	Y
3XMMJ145442.2+182937	0.1163	0145020101	552	N	Y	N	N	Y
3XMMJ145720.4-011102	0.0873	0502780601	75	N	Y	N	Y	Y
3XMMJ150121.9+014401	0.6082	0554680201	2432	N	Y	N	N	Y
		0554680301	1848	N	Y	N	Y	Y
		0302460101	731	N	Y	N	N	Y
3XMMJ150754.3+010817	0.061	0402781001	394	N	Y	Y	N	Y
3XMMJ150946.8+570002	0.0026	0111260201	109	N	Y	Y	N	Y
3XMMJ151106.4+054123	0.0807	0111270201	2746	N	N	N	N	N
		0551780301	3743	N	Y	N	Y	Y
		0551780201	4558	N	Y	N	Y	Y
		0551780501	1949	N	Y	N	Y	Y
		0551780401	4369	N	Y	N	Y	Y
3XMMJ153457.2+233011	0.0181	0101640901	739	Y	Y	N	N	Y
		0205510501	502	Y	N	N	N	Y
		0205510201	340	N	Y	N	N	Y
		0101640801	685	Y	N	N	N	Y
		0205510401	176	N	N	N	N	N
3XMMJ153641.6+543505	0.447	0150610301	111	N	Y	N	Y	Y
		0300310401	374	N	Y	N	N	Y
		0300310501	491	N	Y	N	N	Y
3XMMJ160426.5+174431	0.041	0147210301	375	N	Y	N	N	Y
3XMMJ205017.8-053626	6.0E-4	0203050501	11300	N	Y	N	Y	Y
3XMMJ215649.5-074531	0.0554	0654440101	256	N	Y	N	N	Y
		0404910701	98	N	Y	Y	N	Y

Columns:(1) Source name in the 3XMM-DR4 catalog. (2) Spectroscopic redshift from SDSS-DR7. (3) Observation identifier in 3XMM-DR4. (4) Counts collected (all instruments added together) in 0.5-10 keV. (5), (6), (7), and (8): whether or not the automated spectral-fitting results flagged the observation as belonging to each sample. (9) Whether or not the observation fulfill any of the samples criteria.